

Article

IrO_x Supported on Submicron-Sized Anatase TiO₂ as a Catalyst for the Oxygen Evolution Reaction

Josep Boter-Carbonell ^{1,2}, Carlos Calabrés-Casellas ¹, Maria Sarret ¹, Teresa Andreu ^{1,*} and Pere L. Cabot ^{2,*}

¹ Sustainable Electrochemical Processes Group (SEP), Institute of Nanoscience and Nanotechnology (IN2UB), Universitat de Barcelona, Martí i Franquès 1-11, 08028 Barcelona, Spain; j.boterc@ub.edu (J.B.-C.); ccalabca7@alumnes.ub.edu (C.C.-C.); m.sarret@ub.edu (M.S.)

² Laboratory of Electrochemistry of Materials and the Environment (LEMMA), Department of Materials Science and Physical Chemistry, Universitat de Barcelona, Martí i Franquès 1-11, 08028 Barcelona, Spain

* Correspondence: tandreu@ub.edu (T.A.); p.cabot@ub.edu (P.L.C.)

Abstract: Ir-based catalysts are the best in terms of activity and stability for oxygen evolution reactions (OERs) in proton exchange water electrolysis. Due to their cost, efforts have been made to decrease their load without a loss of activity. In this paper, Ir nanoparticles measuring 2–3 nm were loaded on TiO₂ anatase supports of submicrometric size in different amounts using the microwave polyol method to optimize their mass activity. Using anatase particles with a diameter of about 100 nm and titania nanotubes (TNTs), Ir/TiO₂ catalysts with Ir contents of 5, 10, 20, and 40 wt.% were synthesized and characterized via structural and electrochemical techniques. It was shown that the amount of Ir must be regulated to obtain continuous coverage on titania with strong Ir–TiO₂ interactions which, for the 100 nm diameter anatase, is limited to about 20 wt.%. A higher percentage of Ir over 40 wt.% can be dispersed over the TNTs. Exceeding one layer of coverage leads to a decrease in the catalyst's utilization. Ir/TiO₂(10:90), Ir/TiO₂(20:80), and Ir/TiO₂(40:60) presented the highest pseudocapacitive currents per unit of Ir mass. The electrochemical active areas and mass activities for these later catalysts were also the highest compared to Ir/TiO₂(05:95), Ir/TNT(40:60), and the unsupported catalysts and increased from 40 to 10 wt.% Ir. They also presented the lowest overpotentials of about 300 mV at 10 mA cm^{−2} for the OER, with Ir/TiO₂(10:90) presenting the best specific activities and surface turnover frequencies, thus showing that the size of the support can be regulated to decrease the Ir content of the catalyst without a loss of activity.

Keywords: iridium oxide; oxygen evolution reaction; strong metal–support interaction; supported catalysts; anatase TiO₂ supports; titania nanotubes; water electrolyzers



Academic Editors: Yurii V. Geletii and Tam D. Nguyen

Received: 11 December 2024

Revised: 2 January 2025

Accepted: 5 January 2025

Published: 16 January 2025

Citation: Boter-Carbonell, J.; Calabrés-Casellas, C.; Sarret, M.; Andreu, T.; Cabot, P.L. IrO_x Supported on Submicron-Sized Anatase TiO₂ as a Catalyst for the Oxygen Evolution Reaction. *Catalysts* **2025**, *15*, 79. <https://doi.org/10.3390/catal15010079>

Copyright: © 2025 by the authors. Licensee MDPI, Basel, Switzerland. This article is an open access article distributed under the terms and conditions of the Creative Commons Attribution (CC BY) license (<https://creativecommons.org/licenses/by/4.0/>).

1. Introduction

H₂ is a high-specific-energy fuel destined to be an essential energy vector in the future, helping minimize the environmental impact caused by the use of fossil fuels [1,2]. The combustion of pure H₂ leads to pure H₂O. However, H₂ is currently mostly produced from non-renewable sources, such as methane reforming or coal gasification, which lead to CO₂ generation and environmental pollution [3]. H₂ can also be obtained by water splitting, which, when performed using renewable energy sources such as photovoltaic or wind energy, is called green hydrogen, as these processes do not generate CO₂ emissions [4,5].

Hydrogen can be produced using a variety of methods, although only those based on water splitting, such as electrolysis, thermolysis, and photoelectrolysis, can lead to pure H₂, with O₂ as the only by-product [3]. Electrolysis is a proven and efficient technology.

Nevertheless, it is limited by its cost, since the sluggish four-electron oxygen evolution reaction (OER) requires the use of precious metal catalysts [6–10], and only approximately 4% of H₂ is produced in this way, mainly in the food and semiconductor industries [11,12].

Alkaline water electrolysis is an established technology. However, it is limited to a low partial load range, carbonate formation problems, low pressure, and small current densities [13]. Comparatively, proton-exchange membrane water electrolyzers (PEMWEs) are compact systems; they use low-resistance proton-conducting polymer electrolytes with low H₂ permeability, and the gasses evolve at the back of the electrodes. Thus, they can produce high-purity H₂ at higher pressures and current densities; this has been the object of recent studies in the literature [11–19]. Comparatively, anion exchange membranes for alkaline electrolysis are still under development [11]. A limitation of PEMWEs is that they use proton exchange membranes (PEMs) as electrolytes, which are acidic in nature and therefore require corrosion-resistant noble metals as catalysts [20]. It has been found that one of the most active catalysts for the OER is RuO₂, but it has low stability under acidic conditions and therefore reduces the lifetime of the electrolyzers [21,22]. IrO_x is preferred because it is more stable and has very favorable catalytic properties for the OER [23]. However, the price of Ir is very high at 146.29 USD g_{Ir}⁻¹ [24]. Since it is an extremely rare and expensive precious metal, the use of Ir increases the economic cost of the electrolyzer [25].

The use of IrO₂ at 2.10 mg cm⁻² loading enabled a current density of 6.0 A cm⁻² in a PEMWE at 1.80 V and 80 °C [14]. To the best of the authors' knowledge, this value is among the highest reported, and it can be considered a benchmark. However, the amount of Ir employed is too high. In recent years, the possibility of synthesizing IrO_x nanoparticles on different supports has been studied, aiming to reduce the amount of Ir required while enhancing metal's utilization and the catalyst's stability [26–29]. A key point appears to be the catalyst–support interaction, which allows for an increase in the catalyst's activity and stability due to their mutual electronic interactions [30–32]. Some supports providing the best results are those based on SnO₂ and TiO₂, which demonstrate high corrosion resistance in acidic media [33,34]. Between them, TiO₂ is especially promising for large-scale applications given its stability, abundance, low cost, and established production technology. Although it is a semiconductor with a significant bandgap, its conductivity can be improved through doping with metallic and non-metallic elements [30,35–37]. Current densities of 1 A cm⁻² have been reported at 1.73 and 1.67 V at 80 °C for Ir loadings of 0.12 and 0.4 mg_{Ir} cm⁻², respectively, using a physical mixture of IrO₂ with Ti microparticles [27] and rutile TiO₂ core microparticles covered by an IrO₂ shell [28], both using 50 wt.% IrO₂ with respect to the supported catalysts. These findings demonstrate the need for a support to decrease the required precious metal loading.

The present work is focused on the synthesis of Ir-based nanoparticles deposited over TiO₂ in an anatase polymorphic structure. Anatase TiO₂ allows the formation of different heterostructures, such as nanotubes, spheres, or cubes, and the dispersal of iridium nanoparticles over different morphologies, ensuring a homogeneous and continuous distribution and avoiding agglomerations [38–40]. When using the supported catalysts, the wt.% of IrO₂ is normally high and depends on the nature and size of the support [28,29]. The current literature shows that it is possible to reduce the IrO₂ content up to about 40 wt.% with increased activity [30,36,41–43]. In this paper, we examine the possibility of a further decrease in the wt.% of iridium on the supported catalysts, maintaining or even improving their catalytic activity, using submicrometric anatase TiO₂ particles and a facile synthesis procedure. The selected anatase supports were commercially available titania spheres of about 100 nm in size and synthesized titania nanotubes (TNTs). The supported catalysts were characterized using scanning electron microscopy (SEM), transmission elec-

tron microscopy (TEM), energy-dispersive X-ray spectroscopy (EDS), X-ray photoelectron spectroscopy (XPS), cyclic voltammetry (CV), and linear sweep voltammetry (LSV). The catalytic activity and accelerated stability tests of the synthesized catalysts were carried out, the results of which were compared with those obtained using synthesized Ir nanoparticles and commercial Ir Black, especially for PEMWEs, as a reference.

2. Results

2.1. Physicochemical Characterization

The synthesized TNTs were examined via Raman spectroscopy to determine whether they presented the same polymorphic form as that of commercial anatase TiO₂. Figure S1a in the Supplementary Material shows that the synthesized TNTs present four peaks, which correspond to the normal vibration modes with symmetries E_g at 144 and 636 cm⁻¹, B_{1g} at 394 cm⁻¹, and A_{1g} at 514 cm⁻¹ [44], which are the same as those of the commercial anatase. These peaks clearly correspond to TiO₂ with an anatase conformation, thus indicating that the synthesis method successfully yielded to the desired supporting material [45]. These supports were also examined by X-ray diffraction (XRD), as shown in the Supplementary Material (Figure S1b), confirming that they were only anatase. In addition, XRD allowed the mean crystallite size to be determined, which was 33 and 67 nm for the TNTs and commercial TiO₂, respectively.

It is expected that the deposited iridium covers the titania's surface during the synthesis process. This is confirmed by the Ir EDS mapping presented in Figure 1, which shows that the Ir is quite homogeneously distributed over the titania support.

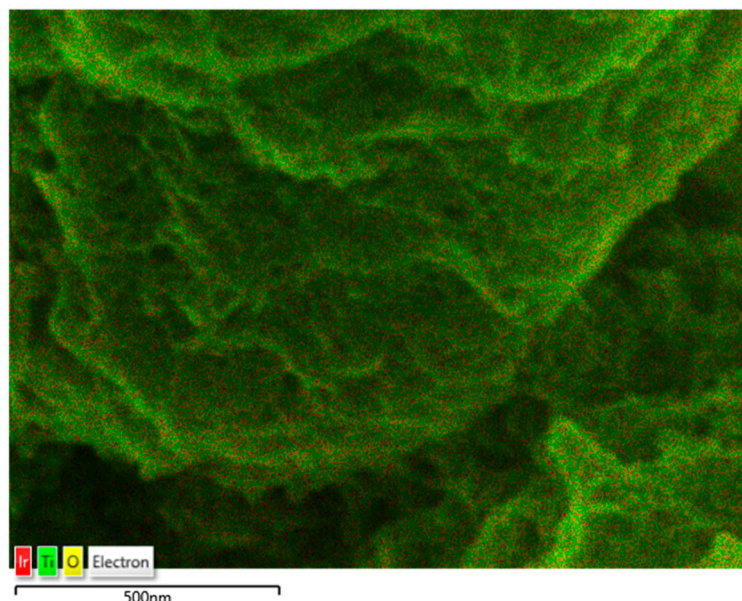


Figure 1. EDS mapping of Ir obtained for the synthesized Ir/TNT(40:60) sample.

Table 1 shows the composition of Ir and TiO₂ in the Ir/TiO₂ and Ir/TNT samples prepared in the microwave reactor, determined from the EDS spectra, where TiO₂ refers to the commercial anatase and TNT to the synthesized titania nanotubes, as described in Section 3. For the commercial anatase, the Ir composition corresponds to the stoichiometrically calculated value, indicated in parentheses. However, there is a strong deviation for Ir/TiO₂(20:80) and Ir/TiO₂(40:60), and these deviations are greater when higher amounts of Ir are deposited. It is therefore apparent that a significant Ir detachment for the latter samples took place during the synthesis because the commercial anatase particles could not retain the greater amount of Ir over their surface, thus only supporting a limited amount of

Ir. Note, however, that the amount Ir in the Ir/TNT(40:60) sample is close to the stoichiometric value, which is notably higher than that of Ir/TiO₂(40:60). This can be attributed to the different specific surface areas of the commercial anatase and that of the TNTs, which are greater in the latter.

Table 1. Ir/TiO₂ wt.% ratio in the supported catalysts.

| Sample | Ir/wt.% | TiO ₂ /wt.% |
|-----------------------------|---------|------------------------|
| Ir/TiO ₂ (05:95) | 5 ± 1 | 95 ± 1 |
| Ir/TiO ₂ (10:90) | 10 ± 2 | 90 ± 2 |
| Ir/TiO ₂ (20:80) | 15 ± 2 | 85 ± 2 |
| Ir/TiO ₂ (40:60) | 28 ± 2 | 72 ± 2 |
| Ir/TNT(40:60) | 38 ± 2 | 62 ± 2 |

The percentage values have been calculated assuming that all the Ti is in the form of TiO₂ and all the Ir is in its metallic form.

The SEM results are complemented by the TEM micrographs depicted in Figure 2. Figure 2a,b display TEM images of the catalysts with 5 and 10 wt.% Ir, respectively. They also show the uniform dispersion of the Ir NPs on the TiO₂ surface. DigitalMicrographTM software version 3.7.4 enabled the particle sizes of Ir and TiO₂ to be measured, and it was found that the particle size of Ir is about 2.5 ± 0.5 nm while that of the commercial anatase is about 100 ± 20 nm; these particle sizes match reasonably well with the values obtained from the XRD analyses. In contrast, the TEM images in Figure 2c,d, which correspond to 20 and 40 wt.% Ir, show loose Ir agglomerates; this finding is in agreement with the results of the EDS analyses (Table 1), suggesting the detachment of Ir particles from the TiO₂ surface during the synthesis because the anatase is not able to support all the deposited Ir. Conversely, the amount of 40 wt.% Ir dispersed on the TNTs (given in Table 1) is supported by the titania, and the results of the EDS analysis match the prepared stoichiometry; moreover, the TEM image in Figure 2e reveals that there is still free titania surface available for further Ir coverage. Note that the Ir agglomerates on the supported catalysts in Figure 2c,d look similar to the Ir NPs shown in Figure 2f, which have been synthesized in the same form but without any supports. The TEM micrograph of commercial Ir Black is shown in the Supplementary Material Figure S2 and appears to consist of larger particles which are even more agglomerated.

The hypothesis that the excessive amount of Ir leads to the complete coverage of the anatase spheres in some of the Ir/TiO₂ catalysts can be supported by simple calculations. These calculations allow the Ir-to-TiO₂ ratio to be estimated based on the geometric forms and densities and are reported in the Supplementary Material (Figure S3, Equation (S1), and Table S1). As determined by the TEM observations, the commercial anatase can be represented by spheres 80–100 nm in diameter and the titania nanotubes by cylinders 55–60 nm in length and 8.5–9 nm in diameter. The available area of TiO₂ to immobilize Ir nanoparticles of 2–3 nm in size can be calculated from these geometries. Considering a compact hexagonal distribution of the Ir nanoparticles, it is possible to calculate the Ir volume available on the support's surface, and from the Ir and TiO₂ densities, the weight ratio between both components can be obtained as well. The corresponding results, listed in Table S1, demonstrate that an estimated 20 wt.% Ir loading with an average Ir nanoparticle size of 2 nm corresponds to an almost completely covered surface and that the 40 wt.% Ir loading far exceeds the amount needed for the complete coverage of the TiO₂ particles. However, it is still feasible to synthesize TNTs with the nominal 40 wt.% Ir loading with a significant amount of uncovered surface area remaining. These estimations strongly match with the TEM observations.

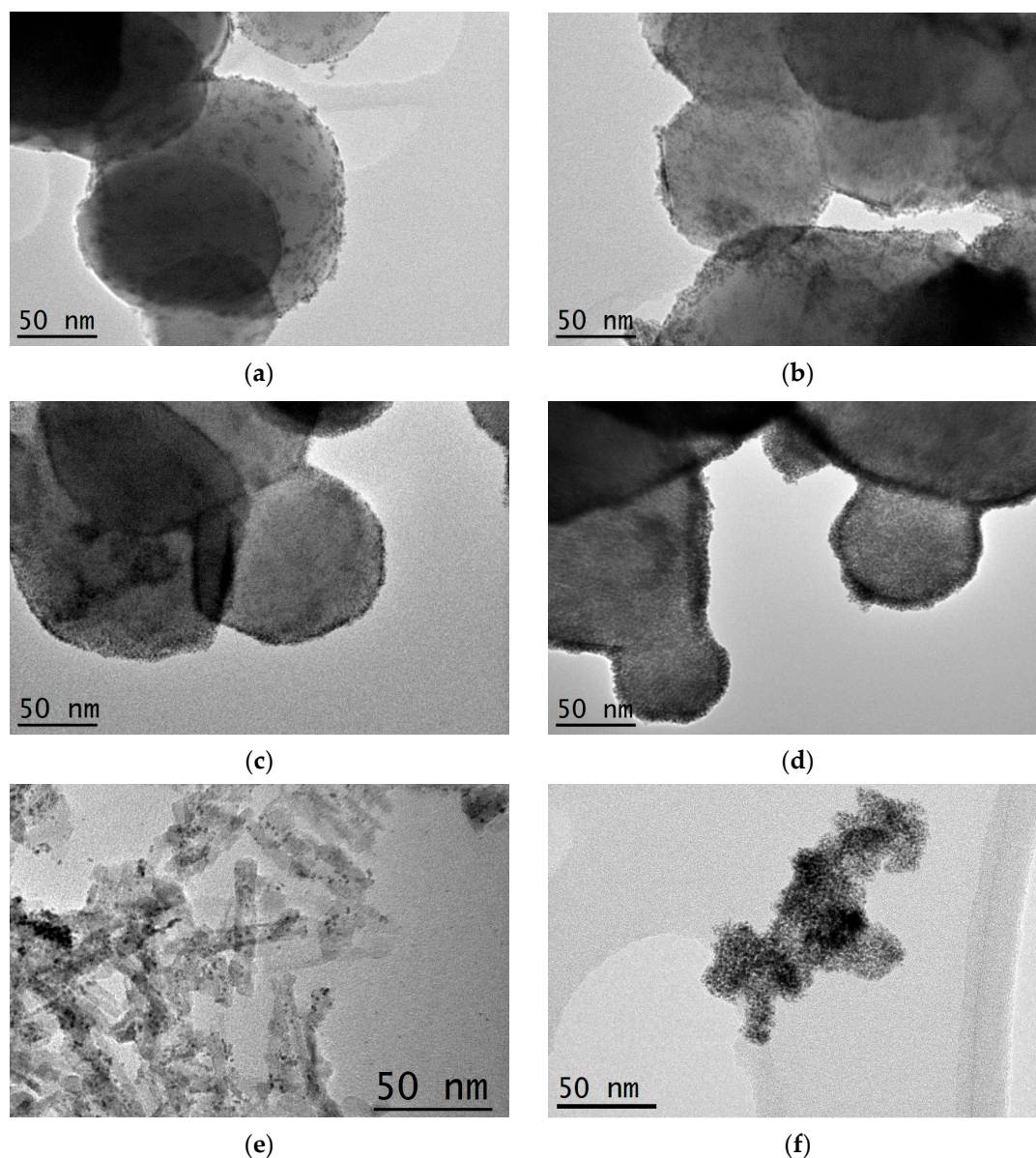


Figure 2. Selected TEM images of the different supported catalysts: (a) Ir/TiO₂(05:95); (b) Ir/TiO₂(10:90); (c) Ir/TiO₂(20:80); (d) Ir/TiO₂(40:60); (e) Ir/TNT(40:60); and (f) Ir NPs.

The chemical state of Ir compared to that of commercial Ir Black has been studied via XPS analysis of the supported catalysts (Figure 3). The doublets of Ir 4f, due to the spin-orbit split, are identified as 4f_{7/2} and 4f_{5/2}. Importantly, the two Ir 4f peaks in the catalyst and in Ir Black do not appear at the same binding energy (BE). These peaks have been deconvoluted in both samples, with the results shown in the same figures. The best deconvolution for Ir Black is obtained when considering the metallic Ir (Ir⁰) and the oxidized Ir in the Ir oxide as IrO_x. In this case, the corresponding BEs of Ir⁰ are 61.1 and 64.2 eV, while in the case of Ir in the form of IrO_x, they are 62.6 and 65.7 eV. These values are in agreement with previous data reported in the literature [43,46,47]. The XPS analyses of the supported catalyst give the same BEs of 61.1 and 64.2 eV for Ir⁰. However, the BEs for Ir in the form of IrO_x are 62.2 and 65.3 eV, which are 0.4 eV lower than those of Ir Black and reasonably match with previously reported results obtained using the same synthesis procedure, although for another support metal [43]. This means that there is an IrO_x-TiO₂ interaction that leads to a partial transfer of negative charge from the support to the Ir in IrO_x, which has been described as enhancing the OER and the stability of IrO₂@Ir/TiN [43].

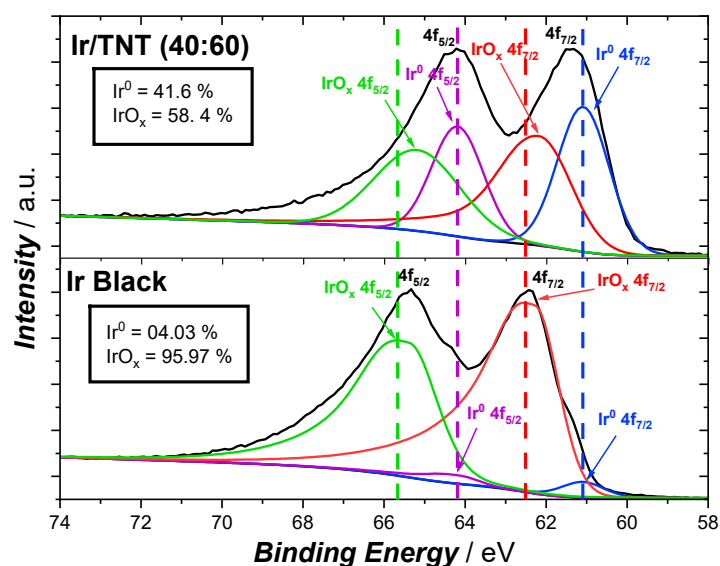


Figure 3. Deconvoluted XPS spectrum of the synthesized Ir/TNT(40:60) catalyst compared to that of Ir Black. The different color dashed lines show the shift of some of the binding energy peaks.

Deconvolution also allows the relative amounts of Ir⁰ and oxidized Ir in the form of IrO_x in both samples to be determined, showing that most of the Ir Black is IrO_x (95.97 at.% Ir), with only 4.03 at.% Ir⁰. Conversely, 41.6 at.% iridium is in the form of Ir⁰ in Ir/TNT(40:60), meaning that the latter is composed of metallic Ir and oxidized Ir in the form of IrO_x, which was previously assigned to the poor reduction capacity of ethylene glycol in the synthesis conditions [43,48]. Due to this composition and small size, no crystalline structure for Ir⁰ or IrO_x was expected. In fact, the composition and size are comparable to those reported in a previous work using the same synthesis procedure, in which no crystalline nature was detected for the Ir species deposited on TiN, neither by TEM electron diffraction nor by XRD [43], thus implying that they were amorphous [43]. Note in addition that this Ir-to-IrO_x ratio could change when activating the catalyst prior to being applied to the OER.

2.2. Electrochemical Performance

After the physicochemical characterization of the synthesized materials, their pseudo-capacitive and catalytic properties were studied in acidic media to simulate the reaction conditions in a PEMWE. Note, however, as observed from the XPS results, that most of the supported Ir resulting from the microwave synthesis is in its metallic form. To obtain IrO₂, which is the main catalytic species, the catalyst is activated by potential cycling in the range of 1.0–1.6 V, as indicated in Section 3 [8,11,43]. The increase in current density observed during activation up to a steady cyclic voltammogram suggests the Ir surface's transformation into a suitable oxidation state.

2.2.1. Pseudocapacitance Analyses of the Catalysts

The steady cyclic voltammograms in the potential range of 0.1–1.4 V at 200 mV s⁻¹ in deaerated and steady 0.1 M HClO₄ for the different catalysts studied are shown in Figure 4, the current densities being normalized to the Ir mass (j_N) with respect to the electrode potential. The cyclic voltammograms for the Ir NPs (80 μg cm⁻²) and Ir Black have also been included for comparison.

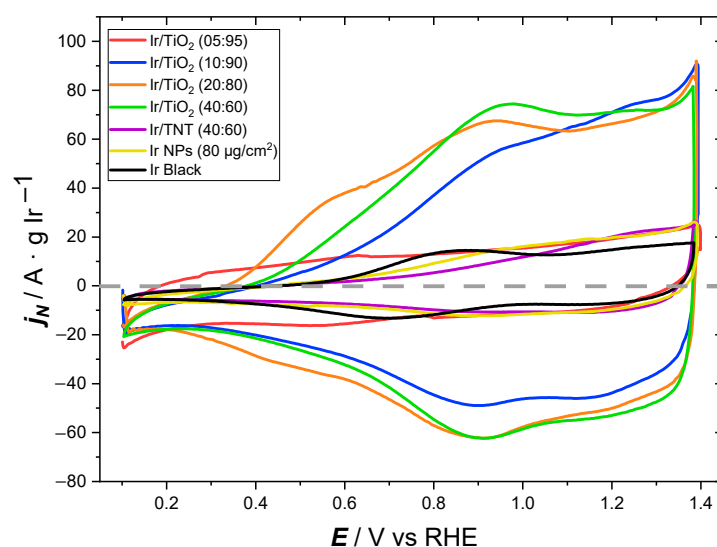


Figure 4. Steady cyclic voltammograms at 200 mV s^{-1} of the different catalysts, normalized to the mass unit of Ir, in deaerated 0.1 M HClO_4 .

According to the literature, the potential region between 0.1 and 0.4 V corresponds to the atomic hydrogen desorption/absorption processes (anodic/cathodic sweeps, respectively) [36,49,50]. At potentials above 0.4 V, the adsorption/desorption of OH on the catalyst and the redox transitions of the oxidized Ir species take place. The anodic and cathodic peaks at about 0.9 V can be attributed to the reversible Ir(IV)/Ir(III) couple, whereas a transition to a higher oxidation state from Ir(IV) to Ir(>IV) appears over 1.2 V [49,51,52]. Cyclic voltammograms at the different scan rates for all the catalysts referred to in Section 3 are plotted in Figure S4 of the Supplementary Material. It is shown that the redox peaks of the Ir(IV)/Ir(III) couple flatten out when decreasing the Ir content in the supported catalyst, i.e., from 40 (Figure S4d) to 5 wt.% (Figure S4a). This flattening out has been interpreted to be the consequence of the positive Ir interaction with the support, which stabilizes the Ir(III) oxidation state and increases the catalyst's stability [53]. The greater the interaction between Ir and the support, the greater the expected flattening of the peaks; thus, less flattening is observed for the highest Ir content, in which more Ir agglomerates are formed and less Ir appears to be stabilized on the support. Note that these peaks are less marked for Ir/TNT(40:60) (Figure S4e) because having a larger surface area allows a greater amount of Ir to be stabilized. Conversely, the Ir(IV)/Ir(III) peaks for Ir Black are quite well defined (Figure S4g).

Note that the form of the cyclic voltammograms of Ir/TiO₂(05:95) significantly differs from that of the other catalysts. This seems to be related to an insufficient amount of Ir coverage, as these voltammograms practically do not exhibit the reversible peak at 0.9 V and thus the response of the TiO₂ support can be overlapped, as shown in the curves depicted in Figure S4a,h of the Supporting Material. It can be observed that the anodic and cathodic features of the cyclic voltammograms of Figure S4h, which correspond to TiO₂, appear in those of Ir/TiO₂(05:95) (Figure S4a). All the other supported catalysts present reversible peaks, with anodic and cathodic peaks at the same potential of 0.9 V, suggesting that the electron transfer is very fast, probably facilitated by the strong metal–support interaction. In the case of Ir Black (Figure S4g), the anodic and cathodic peak potentials are significantly different, with the anodic ones shifting slightly in the positive direction to approach 0.9 V, whereas the cathodic ones move to 0.7 V. This indicates that the peak potentials are quasireversible for this catalyst, with a slower electron transfer process in the film [54]. On the contrary, the peak potential of the Ir NPs does not significantly depend on the scan rate (Figure S4f), suggesting a faster electron transfer. Note, however, that the NPs

were synthesized in the same form as that of the supported materials, which could lead to more suitable structural characteristics than reversibility.

The curves shown in Figure 4 can be associated with pseudocapacitive behavior with a high charge storage capacity [55]. The corresponding overall anodic and cathodic charges can thus be related to the specific surface area of the different catalysts. The overall charge presents two contributions: the outer surface charge (fast process) and the intercalation one (slow diffusion process). The fast (or outer) charge, denoted as q_{outer} , corresponds to the most accessible active sites at high scan rates. On the other hand, the overall charge, or q_{total} , involves all the active sites, including those in the regions that are not accessible at high scan rates but which become accessible at lower scan rates. The charge exchange between surface OH groups and the acidic electrolyte is rapid in easily accessible regions but faces diffusion limitations in the inner regions, where the charged species can be intercalated. Measuring the overall anodic and cathodic charges at different scan rates allows the outer and total charge of the electrode to be determined [36,55–57]. To determine q_{outer} and q_{total} , one can plot the integrated total charge (q) at a given scan rate against the inverse square root of the scan rate ($v^{1/2}$) (Equation (1)) and the inverse of q in the case of ($v^{1/2}$) (Equation (2)), respectively:

$$q = q_{\text{outer}} + k' \left(\frac{1}{v^{1/2}} \right) \quad (1)$$

$$\frac{1}{q} = \frac{1}{q_{\text{total}}} + k'' (v^{1/2}) \quad (2)$$

where k' and k'' correspond to two reaction constants. From q_{outer} and q_{total} , the value of q_{inner} , the charge corresponding to the less accessible active sites of the catalyst for the reaction to take place, can be calculated (Equation (3)):

$$q_{\text{inner}} = q_{\text{total}} - q_{\text{outer}} \quad (3)$$

The graphs generated to determine all charges for the different catalysts are reported in a supplementary file, Figure S5a–n. Note that the calculations have been performed considering the integrated total anodic charge (q_{anodic}) and the integrated total cathodic charge (q_{cathodic}) separately. The corresponding results are listed in Table 2.

Table 2. Outer (q_{outer}), inner (q_{inner}), and total (q_{total}) charges of the IrO₂ catalysts, measured from the cyclic voltammograms shown in Figure S5a–n of the Supplementary Material.

| Catalyst | q_{outer} (μC) | q_{inner} (μC) | q_{total} (μC) | | Reversibility ($q_{\text{anodic}}/q_{\text{cathodic}}$) | Accessibility ($q_{\text{outer}}/q_{\text{total}}$) |
|--|--------------------------------------|--------------------------------------|--------------------------------------|-----------------------|--|--|
| | | | q_{anodic} | q_{cathodic} | | |
| Ir/TiO ₂ (05:95) | 44 | 69 | 113 | −128 | 0.88 | 0.63 |
| Ir/TiO ₂ (10:90) | 279 | 267 | 546 | −528 | 1.03 | 0.51 |
| Ir/TiO ₂ (20:80) | 499 | 339 | 838 | −824 | 1.02 | 0.59 |
| Ir/TiO ₂ (40:60) | 670 | 1841 | 2511 | −2576 | 0.97 | 0.27 |
| Ir/TNT(40:60) | 221 | 440 | 661 | −640 | 1.03 | 0.33 |
| Ir NPs (80 $\mu\text{g}/\text{cm}^2$) | 251 | 523 | 773 | −746 | 1.04 | 0.32 |
| Ir Black | 590 | 683 | 1273 | −1280 | 0.99 | 0.46 |

When analyzing the redox couple Ir(IV)/Ir(III) in Figure 4, a horizontal symmetry can be observed, in agreement with the reversibility of the process. This reversibility can be quantitatively confirmed as the ratio $q_{\text{anodic}}/q_{\text{cathodic}}$, given in Table 2, which is close to unity in all cases, except for the supported catalyst with the lowest Ir content, which

significantly deviates from this value. This is not surprising because the Ir/TiO₂(05:95) voltammograms show the overlapping of TiO₂, as explained before.

On the other hand, the $q_{\text{outer}}/q_{\text{total}}$ ratio indicates the accessibility of the surface groups to sustain the reaction. As shown in Table 2, the supported catalysts have, in general, a higher accessibility, so less of the catalyst appears in its more occluded form. In the case of Ir/TiO₂(40:60), the transport of the species could be limited by the agglomerates formed, which are apparent in Figure 2d. The same explanation could be applied to the Ir NPs and Ir Black, since the unsupported catalyst appears to be agglomerated, as shown in Figure 2f. Ir/TNT(40:60) exhibits a higher surface area than the commercial anatase, together with a superposition of nanotubes and, for this reason, the accessibility could also be partially limited. The general conclusion is that extending the Ir nanoparticles over the support with a small agglomeration helps to expose the active sites available for the OER.

In relation to the accessibility of the active sites of the supported catalysts, the electrochemical active surface area (ECSA) is also of interest. To obtain the values of the ECSAs, the double layer capacity (C_{dl}) values were first determined. They were calculated as the slope of the capacitive current density j_c at 1.05 V, which is the minimum value between the Ir(III) and the Ir(IV) transitions (see Figure S4g in the Supplementary Material) with respect to the sweep rate v (Equation (4)) [58,59]:

$$j_c = C_{\text{dl}}v \quad (4)$$

These plots are shown in Figure S6a–g in the Supplementary Material. Note that j_c approaches zero when extrapolating to $v = 0$. After calculating C_{dl} (in $\mu\text{F}\cdot\text{cm}^{-2}$) from these plots, the total active areas of Ir on the RDE tip (A_{aa} , in cm^2) and the corresponding ECSAs ($\text{m}^2 \text{g}_{\text{Ir}}^{-1}$) can be obtained through Equations (5) and (6), respectively:

$$A_{\text{aa}} = \frac{C_{\text{dl}}}{C_s} S_g \quad (5)$$

$$\text{ECSA} = 100 \frac{A_{\text{aa}}}{w_{\text{Ir}} S_g} \quad (6)$$

where C_s is the surface capacity of the smooth Ir catalyst, equal to $350 \mu\text{F}\cdot\text{cm}^{-2}$ [58,59], S_g is the electrode section (0.071 cm^2 , see Section 3.4), and w_{Ir} is the Ir load of the catalyst (the corresponding wt.% Ir of $200 \mu\text{g cm}^{-2}$ (Ir + TiO₂) of the catalyst loading). The factor of 100 expresses the ECSA in the indicated units.

The values of A_{aa} and ECSAs are represented in Figures 5a and b, respectively. The A_{aa} values clearly show that the overall Ir surface area depends on the catalyst. Note that when doubling the catalyst amount, A_{aa} is less than doubled, which indicates catalyst agglomeration in Ir/TiO₂(20:80) and Ir/TiO₂(40:60). Figure 5b depicts the corresponding ECSAs, showing that the Ir/TiO₂(10:90), Ir/TiO₂(20:80), and Ir/TiO₂(40:60) catalysts have all higher ECSAs than the commercial Ir Black, and therefore, they present greater mass activity. Note that the sequence of A_{aa} values differs from that of ECSAs due to the diverse amounts of Ir loading and the variation in the catalyst morphology. Considering the three supported catalysts tested, the lower the supported Ir content, the higher the ECSA value. This indicates that supporting Ir on titania allows for increasing the mass activity of the catalyst and this in turn impacts the OER efficiency, as analyzed in the following subsections.

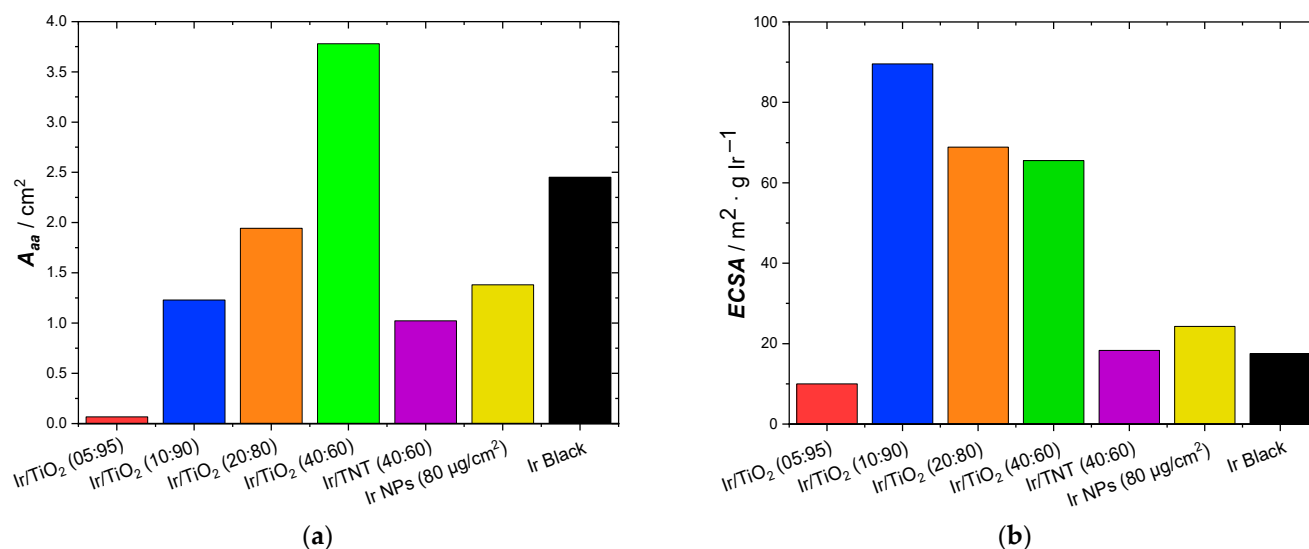


Figure 5. (a) Overall active areas (A_{aa}) on the RDE tip and (b) ECSAs of the different catalysts.

2.2.2. Overpotential for the OER

Figure 6a,b show the linear sweep voltammograms, in linear and semilogarithmic form, respectively, obtained between 1.1 and 1.8 V. From these plots, the overpotential at 10 mA cm^{-2} (η_{10}), the anodic Tafel slopes (b), the current densities (j), the mass (j_m), and the specific activities (j_s), together with the surface turnover frequencies (TOFs) at 1.525 V, which are circa 300 mV over the equilibrium potential, are obtained. All these data, collected in Table 3, reveal the activities of the different catalysts studied and allow their comparison.

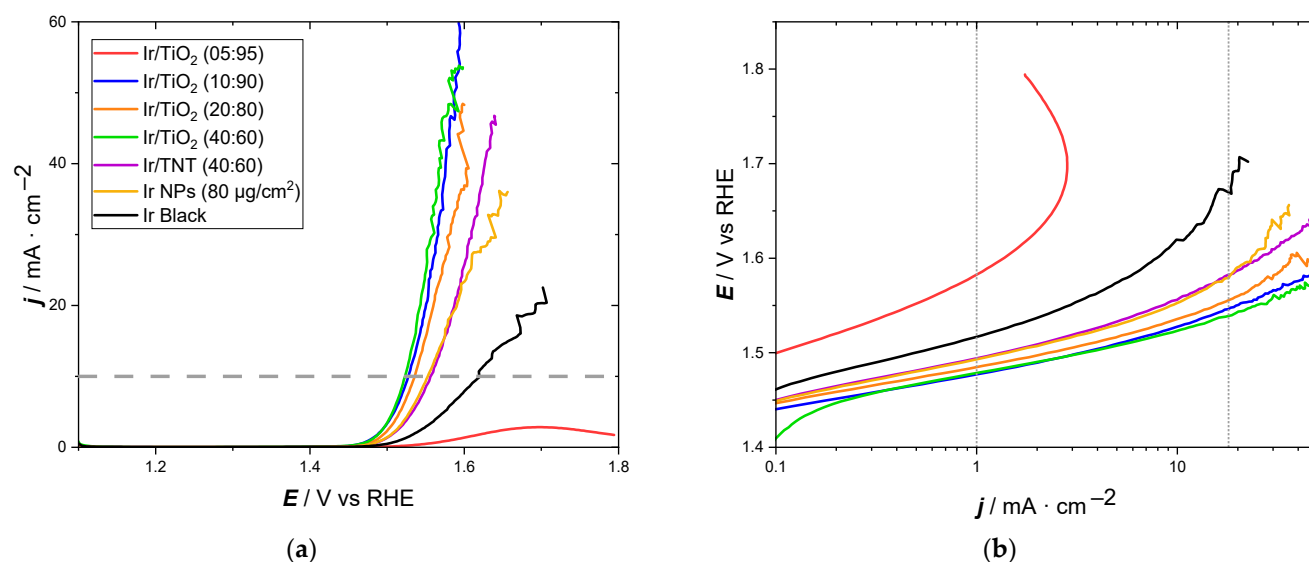


Figure 6. (a) Linear sweep voltammograms of the catalysts in deaerated 0.1 M HClO₄ at 1 mV s^{-1} . (b) Tafel plots corresponding to the voltammograms plotted in (a). The grey dashed line in (a) has been depicted to compare the overpotentials of the different catalysts at 10 mA cm^{-2} . The grey dashed lines in (b) indicate the current densities at which the Tafel lines were drawn.

Table 3. Representative magnitudes of the electrocatalysts' performances: overpotential at 10 mA cm⁻² (η_{10}); Tafel slopes in the low ($b_{low j}$) and high j ($b_{high j}$) regions; current density refers to the electrode section (j), mass activity (j_m), specific activity (j_{sp}), and surface turnover frequency (TOF_s) at 1.525 V.

| Catalyst | η_{10} /mV | $b_{low j}$ /mV dec ⁻¹ | $b_{high j}$ /mV dec ⁻¹ | 1.525 V | | | |
|---------------------------------|--------------------|--------------------------------------|---------------------------------------|-----------------------------|---|--|--------------------------------------|
| | | | | j /mA cm ⁻² | j_m /A g _{Ir} ⁻¹ | j_{sp} /mA cm ⁻² _{Ir} | TOF _s /s ⁻¹ |
| Ir/TiO ₂ (05:95) | N/A | 122 | N/A | 0.23 | 23.0 | 0.14 | 0.140 |
| Ir/TiO ₂ (10:90) | 298 | 40 | 79 | 9.00 | 450 | 0.52 | 0.506 |
| Ir/TiO ₂ (20:80) | 307 | 40 | 88 | 7.17 | 179 | 0.26 | 0.256 |
| Ir/TiO ₂ (40:60) | 294 | 40 | 71 | 11.0 | 138 | 0.21 | 0.201 |
| Ir/TNT(40:60) | 327 | 47 | 111 | 3.77 | 47.1 | 0.26 | 0.255 |
| Ir NPs (80 μg/cm ²) | 324 | 47 | 136 | 4.36 | 54.5 | 0.22 | 0.218 |
| Ir Black | 391 | 60 | 273 | 1.42 | 7.1 | 0.04 | 0.040 |

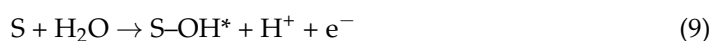
Table 3 shows that the lowest η_{10} overpotentials are obtained for the supported catalysts, with values of circa 300 mV, which are significantly smaller than those for Ir/TNT(40:60), the Ir NPs, and Ir Black. Note that the overpotential of Ir/TiO₂(05:95) is not available because the linear sweep voltammogram does not reach the indicated current density. These values are comparable to recent results reported in the literature of 265 mV for IrO₂@Ir/TiN(60 wt.% Ir) [46], 285 mV for IrO₂/Nb(3%)-TNT(50 wt.% Ir), and 318 mV for IrO_x/Sb:SnO₂(20 wt.% Ir) [48].

The Tafel slopes agree with the overpotentials given because they are smaller for the same catalysts (the smaller the slopes, the smaller the polarization). It is shown in Figure 6b that there is an initial Tafel region, around 1 mA cm⁻² (low j region), in which the Tafel slopes ($b_{low j}$) are about 40 mV dec⁻¹ for the TiO₂-supported catalysts, except for Ir/TiO₂(05:95), which does not meet the suitable catalytic requirements. Somewhat higher $b_{low j}$ values were obtained for Ir/TNT(40:60) and the unsupported catalysts. A second Tafel region at higher current densities ($b_{high j}$) can be appreciated at around 18 mA cm⁻², especially for the supported catalysts. These two Tafel regions in the same current ranges have also been described previously in the literature [36,60–62]. Note that they follow the same trend, being smaller for the TiO₂-supported catalysts.

The Tafel slopes are indicative of the rate determining step (rds) [36,61,63–65]. The following step can be selected in the mechanism:



where S means an active site on the IrO_x. When the rds is Reaction (7), the Tafel slope is 120 mV dec⁻¹, whereas when the rds is Reaction (8), it is 40 mV dec⁻¹. The $b_{low j}$ values match well with those obtained when Reaction (8) is the rds, suggesting that the OH radical rapidly binds to the catalyst. The Tafel slope for Ir Black indicates that in Reaction (7), S-OH* is first produced according to Reaction (9):



where S–OH* is an unstable species leading to S–OH according to Reaction (10):



When the rds is Reaction (9), the Tafel slope is 120 mV dec^{−1}, and when it is Reaction (10), the Tafel slope is 60 mV dec^{−1}. This strongly suggests that water oxidation on Ir Black occurs when Reaction (10) is the rds. The S–OH* unstable species is rapidly formed, although it is slowly stabilized on the active sites.

The higher Tafel slopes for $b_{\text{low } j}$ are related to a change in the rds, since a higher accumulation of S–OH surface groups is expected and thus the OER can take place under mixed kinetic control through Reactions (7) and (8).

At 1.525 V, the highest j_m values are found for the same TiO₂-supported catalysts. The j_m values of the catalysts presenting the highest activities according to η_{10} and Tafel slopes are one order of magnitude higher than those of Ir/TNT(40:60) and the unsupported catalysts. Consequently, catalyst agglomeration plays an important role because it decreases the active surface area exposed to the electrolyte. With respect to the j_m data given in Table 3, the high values for Ir/TiO₂(10:90), Ir/TiO₂(20:80), and Ir/TiO₂(40:60) must be pointed out. The mass activity of the Ir/TiO₂(40:60)catalyst is comparable to a recently reported value of about 150 A g_{Ir}^{−1} at the same potential of 1.525 V for IrO₂@Ir with an Ir loading of 40 wt.% and supported on nano-TiN (about 20 nm in diameter), the same form as in the present paper [43]. The further increase up to 450 A g_{Ir}^{−1} when decreasing the Ir content up to 10 wt.% shows that the mass activity can be increased by modulating the support size.

Apart from the mass activities, the j_{sp} and TOF_s values are of interest because they reflect the activity of the catalyst loadings per unit surface when these loadings are different. The specific activities can be calculated using Equation (11):

$$j_{\text{sp}} = \frac{j S_g}{A_{\text{aa}}} \quad (11)$$

Moreover, the surface TOF, which can be defined as the rate of O₂ evolution on the surface Ir active sites, expressed as moles of O₂ per at-g of Ir per unit time, can be calculated according to Equation (12) [66]:

$$\text{TOF}_s = \frac{j_{\text{sp}} N_A}{4 F \Gamma_{\text{Ir}}} \quad (12)$$

where j_{sp} is the specific current density at 1.525 V, N_A is the Avogadro constant, 4 is the number of electrons transferred per O₂ molecule, F is the Faraday constant, and Γ_{Ir} is the surface concentration of iridium active sites, which, for Ir(111), is 1.59×10^{19} at m^{−2} [58].

The TOFs values match reasonably well with previous results reported in the literature on IrO₂ nanoparticles synthesized via the Adams fusion method, with values in the range of 0.051–0.61 s^{−1} depending on the particle size, the highest values being obtained with nanoparticles of about 1.7 nm [67,68]. The values of j_{sp} and TOFs both indicate that Ir/TiO₂(10:90) presents the highest surface activity, which can be related to the strong metal–support interaction together with the sufficient coverage of the support from the Ir nanoparticles, as discussed above. When the wt.% Ir increases, the formation of aggregates also increases; moreover, the activity also decreases, approaching the activity found for the Ir NPs, because the aggregates do not present a strong metal–support interaction. The low activity of Ir/TiO₂(05:95) could be due to insufficient TiO₂ coverage, as this results in insufficient contact between the Ir nanoparticles, thus affecting the catalyst's conductivity. In the case of Ir/TNT(40:60), the strong metal–support interaction, together with the incomplete TNT coverage, leads to a surface activity comparable to that of Ir/TiO₂(20:80).

The comparatively low activity of Ir Black can be attributed to its different surface structure, as discussed with the Tafel slopes.

In the calculation of the TOFs, a 100% faradaic efficiency for the OER has been assumed. In fact, it is an interesting value to be measured, as the measurement is normally achieved via extended electrolysis in two-electrode cells for several days, with values over 92% and 97% reported in the literature for the OER [67] and the HER [69], respectively. For this reason, we plan to carry out this long-term electrolysis in further experiments using a two-electrode cell, which are outside the scope of the present paper.

2.2.3. Accelerated Stability Tests

Figure 7 shows the overpotential at 10 mA cm^{-2} in the initial conditions and after 500 and 1000 cycles of the stability tests (ASTs), represented from the left to the right for each catalyst, respectively.

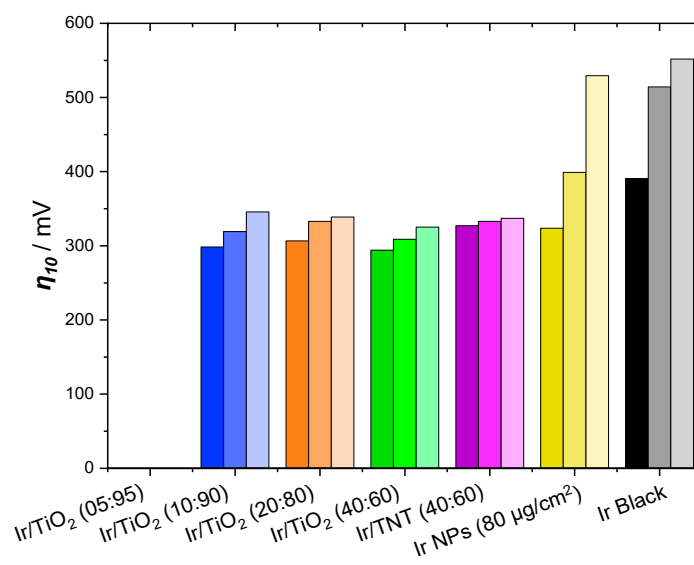


Figure 7. Overpotentials at 10 mA cm^{-2} of the different catalysts during the accelerated degradation tests. Initial value and values after 500 and 1000 cycles between 1.3 and 1.65 V, from the left to the right, for each catalyst.

Except for the catalyst with 5 wt.% Ir, in which the amount of Ir is so low that it does not present significant catalytic properties, the supported materials exhibit a small increase in η_{10} of less than 40 mV. Conversely, the unsupported catalysts show a more important variation of about 200 mV. The increase in the stability of the catalyst when supported can also be explained by the catalyst–support interaction. As previously mentioned, the Ir(IV) in IrO_x accepts negative charges, which is more effective for catalyzing the OER. On the other hand, the unsupported catalysts are more easily oxidized to Ir(>IV), thus diminishing their stability. Consequently, supporting the catalysts on titania allows their useful life to be increased while simultaneously decreasing the metal loading, thus making progress toward reducing the cost of green hydrogen production.

3. Materials and Methods

3.1. Synthesis of Titania Nanotubes (TNTs)

Weighted amounts of 0.75 g of Aeroxide Degussa P25 TiO₂ (Thermo Scientific Chemicals, Madrid, Spain) were dispersed in 75 mL of 10 M NaOH (Panreac AppliChem GmbH, Darmstadt, Germany), magnetically stirred for 2 h, and sonicated for 30 min to ensure a proper dispersion. The solution was then transferred into a hydrothermal polytetrafluoroethylene (PTFE) autoclave reactor and placed in an oven (Memmert UF30 B123.1924,

Fischer Scientific, Madrid, Spain) at 130 °C for 48 h. After the reaction time had elapsed, it was cooled in an ice bath. Subsequently, the dispersion was transferred into centrifuge tubes, where it was successively centrifuged and cleaned with ultrapure water (from Milli-Q Water purification system Merck KGaA, Darmstadt, Germany) until reaching a neutral pH. Afterwards, the dispersion was acidified with 0.1 M HCl (Panreac AppliChem GmbH) to stabilize the pH around 2, and finally, the dispersion was again successively centrifuged and cleaned with ultrapure water to neutral pH. The solid obtained was dried in the oven at 60 °C overnight and then ground in an agate mortar. The obtained powder was transferred to a muffle (Prometheus Kilns Pro-1 PRG, Istanbul, Turkey) and calcined for 2 h and 30 min at 250 °C after a temperature ramp of 5 °C min⁻¹ [37].

3.2. Synthesis of the Titania-Supported IrO₂ Catalyst

A 5 mM aqueous solution of IrCl₃ was prepared from the precursor IrCl₃·H₂O (reagent grade, Merck KGaA). Ethylene glycol (reagent grade, Panreac AppliChem GmbH) was added to prepare a mixture of water/ethylene glycol at a 7:3 volume ratio. Subsequently, variable amounts of commercial anatase TiO₂ or TNTs were added to 16.5 mL of the water/ethylene glycol mixture to obtain different Ir-to-titania ratios. The following specimens were prepared: Ir/TiO₂(05:95), Ir/TiO₂(10:90), Ir/TiO₂(20:80), Ir/TiO₂(40:60), and Ir/TNT(40:60). The values in parentheses refer to the expected wt.% composition in each specimen. An additional catalyst was prepared which was designed as Ir NPs and synthesized in the same form as the supported catalysts with the same amount of IrCl₃ as that used for Ir/TiO₂(40:60) but without the supporting TiO₂. This volume was then introduced in a 30 mL microwave reaction vial, sonicated for 1 min, and placed in a microwave reactor (Monowave 200, Anton Paar GmbH, Madrid, Spain), carrying out the reaction at 140 °C for 20 min [43]. After removal from the reactor, the solid obtained was separated via centrifugation, cleaned several times with water, and finally left to dry in the oven at 60 °C overnight.

3.3. Structural Characterization

Raman spectroscopy was conducted using a Jovin Yvon LabRaman HR800 (Horiba Scientific, Edison, NJ, USA) in the 100–1000 cm⁻¹ range, employing a green laser (532 nm) and using a silicon reference for calibration.

The crystalline structure of the materials and the crystalline field size were analyzed via XRD with a PANalytical Diffractometer X'Pert PRO MPD alpha1 (Malvern Panalytical, Malvern, Enigma Business Park, UK) using a Bragg–Brentano geometry and the monochromated Kα₁ from Cu with λ = 1.5406 Å. The size of the crystalline domain was calculated using the Scherrer equation [70,71]:

$$D = \frac{K \lambda}{\beta \cos \theta} \quad (13)$$

where D is the size of the crystalline domain; K is the shape factor, usually taken as 0.89; λ is the wavelength of the radiation; β is the line broadening at half the maximum intensity (FWHM); and θ is the Bragg diffraction angle.

The samples were observed via field emission SEM (FESEM) using a JEOL J-7100FE microscope (JEOL Ltd., Akishima, Japan), furnished with a Gatan Mono-CL4 spectrometer and an EDS detector, which allowed the Ir/support mass ratio to be determined and facilitated the mapping of the elements. The EDS analyses were performed on six different areas of titania covered with a uniform layer of iridium, thus obtaining the mean value and standard deviation.

The morphology and size of the substrate together with the dispersion and size of the Ir NPs on the supports was studied via TEM using a JEOL JEM 2100 (JEOL Ltd.). The powder to be analyzed was dispersed via sonication in ethanol (reagent grade, Panreac Applichem GmbH). A drop of the dispersion was placed on a holey Ni grid, and the solvent was evaporated using the heat of a lamp. The images were obtained using a Gatan MultiScan 794 CCD camera (Pleasanton, CA, USA) and were digitally treated using Gatan Digital Micrograph 3.7.0 software (Gatan Ametek, Berwyn, PA, USA).

X-Ray photoelectron spectroscopy (XPS) experiments were performed using a scanning photoelectron spectroscope (ESFOSCAN) based on the PHI 5000 VersaProbe 4 Scanning XPS Microprobe from Physical Electronics (ULVAC-PHI, Chanhassen, MN, USA). The measurements were made using a monochromatic focused X-ray source (Aluminum $K\alpha$ line of 1486.6 eV) calibrated using the $3d_{5/2}$ line of Ag with a full width at half maximum (FWHM) of 0.6 eV. The analyzed area was a circle 100 mm in diameter, in which samples were placed at 45° to the analyzer axis, and the selected resolution for the spectra was 224 eV of Pass Energy and 0.8 eV/step for the general spectra and 27 eV of Pass Energy and 0.1 eV/step for the high-resolution spectra of the selected elements. A combination of low-energy electron and ion (Ar^+) guns (both less than 5 eV) was used to discharge samples if necessary. Measurements were referenced to the C 1s signal, whose binding energy is equal to 284.8 eV in adventitious carbon. Measurements were made in an ultra-high vacuum (UHV) chamber at a pressure between 5×10^{-10} and 5×10^{-9} torr. The analysis and fitting of the spectra were carried out with a Physical Electronics Multipak V. 9.9.2. program.

3.4. Electrochemical Characterization

A Princeton Applied Research VMP2 Potentiostat (AMETEK Scientific Instruments, Berwyn, PA, USA) controlled by BioLogic EC-Lab Software version 10.12 (BioLogic GmbH, Göttingen, Germany) was used to perform electrochemical experiments using a conventional three-electrode cell with a software-controlled RDE working electrode (Origabox, SAS OrigaLys ElectroChem, Rillieux-la-Pape, France), an RHE reference electrode (BioLogic), and a graphite bar auxiliary electrode. All the electrode potentials given in this paper have been referred to the RHE. The working electrolyte was 0.1 M $HClO_4$ (reagent grade, Panreac AppliChem GmbH), which was deaerated via Ar bubbling with stirring through the solution and passed over the solution during the electrochemical tests.

The RDE, with a glassy carbon electrode (GCE) tip 3 mm in diameter, was modified by depositing known amounts of the catalyst. Inks consisting of 2–3 mg of catalyst, 400 μ L of Milli-Q water, 200 μ L of 96 vol.% ethanol and 50 μ L of a 5 wt.% Nafion solution in isopropanol (QuinTech The Fuel Cell Supplier, Göppingen, Germany) were prepared. After sonication for 30 min, appropriate volumes of the ink were dropped onto the GCE to obtain catalyst loadings of 200 μ g cm^{-2} (Ir + TiO_2), which were left to dry protected by a capsule. Note that the synthesized Ir NPs were tested with a loading of 80 μ g cm^{-2} , which is the same as that for Ir/ TiO_2 (40:60).

Before obtaining the linear sweep voltammograms in the 1.1–1.8 V potential range at 1 $mV s^{-1}$ and at a rotation rate of 2500 rpm to study the OER, the catalyst was activated via CV, with 20 cycles between 1 and 1.6 V at 100 $mV s^{-1}$ and the same electrode rotation rate [36]. It was observed that the current density slightly increased with time during activation up to a steady voltammogram. The pseudocapacitive properties of the catalyst layers were examined through the steady cyclic voltammograms obtained in the 0.1–1.4 V potential range, so as to avoid the OER, with sweep rates between 20 and 200 $mV s^{-1}$ and in the absence of electrode rotation. The ohmic drop to correct the potentials in the voltammograms was determined via electrochemical impedance spectroscopy (EIS) in an open circuit between 200 kHz and 0.1 Hz and at 10 mV of potential amplitude. The

accelerated tests to study the relative stability of the catalysts consisted of performing 1000 cyclic voltammograms between 1.3 and 1.65 V at 50 mV s⁻¹ with a rotation rate of 2500 rpm [59]. After several hundreds of cycles, LSV curves between 1.1 and 1.8 V were obtained. Parallel experiments using commercial Ir Black (99.8 wt.%, QuinTech, Indiana, PA, USA) as a reference, which is currently used for the OER, were also performed for comparison, also using a catalyst loading of 200 µg cm⁻². This loading was selected because we found the same OER current densities for 400 µg cm⁻², whereas they were smaller for lower loadings.

4. Conclusions

Iridium nanoparticles 2–3 nm in size were deposited at different loadings, from 5 to 40 wt.%, on spherical commercial anatase (80–120 nm in diameter) and on TNTs via the microwave polyol synthesis method with the objective of optimizing the mass activity. SEM and TEM observations, together with EDS analyses and geometrical estimations, showed that the maximum Ir amount that the commercial anatase could support with direct Ir–TiO₂ contact was about 20 wt.%. Due to their different specific surface areas, the TNTs could easily support 40 wt.% Ir. When the Ir content was higher than about 20 wt.%, loosely adhered Ir nanoparticles developed on the adhered catalyst. For 5 wt.% Ir, the amount of catalyst deposited was insufficient because of the lack of continuity and thus conductivity.

According to the XPS analysis and compared to commercial Ir Black, which mainly consists of IrO₂, the Ir nanoparticles deposited via the indicated synthesis procedure contained about 40 at.% Ir⁰ due to the low reduction ability of ethylene glycol. However, a strong IrO_x–TiO₂ interaction with a partial negative charge transfer to Ir(IV) was detected.

The Ir/TiO₂(10:90), Ir/TiO₂(20:80), and Ir/TiO₂(40:60) catalysts presented, after activation, the highest pseudocapacitive current densities and ECSAs, thus indicating the efficiency of using these catalysts instead of Ir/TiO₂(05:95), Ir/TiNT(40:60), Ir NPs, and commercial IrO₂. The developed catalysts also demonstrated sufficient coverage of TiO₂ by the loaded Ir, presenting a suitable conductivity and IrO_x–TiO₂ interaction; these activities are beneficial for enhancing the specimens' catalytic activity for the OER, with current densities of 10 mA cm⁻² with respect to the electrode at overpotentials of about 300 mV. Moreover, these results can be compared to results previously reported in the literature. Higher overpotentials were obtained for the latter. The Ir/TiO₂(10:90) catalyst presented the highest specific activity of 0.52 mA cm_{Ir}⁻² and a turnover frequency of 0.51 s⁻¹, demonstrating the effect of the strong IrO_x–TiO₂ interaction. In addition, the mass activity increased to 450 A g_{Ir}⁻¹ at 1.525 V when decreasing the Ir content from 40 to 10 wt.%, thus showing that the mass activity can be increased by modulating the support size.

The accelerated degradation tests also showed the positive effect of the IrO_x–TiO₂ interaction for Ir/TiO₂(10:90), Ir/TiO₂(20:80), Ir/TiO₂(40:60), and Ir/TNT(40:60). Since there was only a small change in the overpotential at 10 mA cm⁻² after 1000 cycles, the unsupported materials presented a much higher overpotential increase. Therefore, using a titania support can enhance the catalytic activity of a specimen together with its stability during the OER.

Supplementary Materials: The following supporting information can be downloaded at: <https://www.mdpi.com/article/10.3390/catal15010079/s1>. Figure S1. (a) Raman spectra and (b) XRD patterns of the synthesized titania nanotubes (TNTs) and of the commercial anatase TiO₂ used as supports. The peaks at 2θ = 25.3 deg (°), representing β values (in 2θ deg (°)) of 0.256 and 0.128 for TNTs and TiO₂, respectively, were taken to determine the crystallite sizes using the Scherrer equation. Figure S2. TEM image of the commercial Ir Black catalyst. Figure S3. Model to estimate the TiO₂ available area to immobilize the Ir nanoparticle. Table S1. Estimation of the maximum iridium loading on the TiO₂ anatase and TNTs. Figure S4. Cyclic voltammograms of the catalysts

at different scan rates: (a) Ir/TiO₂(05:95), (b) Ir/TiO₂(10:90), (c) Ir/TiO₂(20:80), (d) Ir/TiO₂(40:60), (e) Ir/TiO₂(40:60), (f) Ir NPs, (g) Ir Black, and (h) TiO₂ support. Figure S5. Linear plots to determine q_{outer} : (a) Ir/TiO₂(05:95), (c) Ir/TiO₂(10:90), (e) Ir/TiO₂(20:80), (g) Ir/TiO₂(40:60), (i) Ir/TiO₂(40:60), (k) Ir NPs, and (m) Ir Black and q_{total} : (b) Ir/TiO₂(05:95), (d) Ir/TiO₂(10:90), (f) Ir/TiO₂(20:80), (h) Ir/TiO₂(40:60), (j) Ir/TiO₂(40:60), (l) Ir NPs, and (n) Ir Black. Figure S6. Linear plots to determine C_{dl} to obtain the ECSAs: (a) Ir/TiO₂(05:95), (b) Ir/TiO₂(10:90), (c) Ir/TiO₂(20:80), (d) Ir/TiO₂(40:60), (e) Ir/TiO₂(40:60), (f) Ir NPs, and (g) Ir Black.

Author Contributions: Conceptualization, P.L.C. and T.A.; methodology, P.L.C. and T.A.; validation, J.B.-C. and C.C.-C.; formal analysis, P.L.C., M.S. and T.A.; investigation, J.B.-C. and C.C.-C.; resources, T.A. and M.S.; data curation, T.A.; writing—original draft preparation, J.B.-C. and C.C.-C.; writing—review and editing, P.L.C. and T.A.; visualization, P.L.C., M.S. and T.A.; supervision, P.L.C. and T.A.; project administration, T.A. and M.S.; funding acquisition, T.A. All authors have read and agreed to the published version of the manuscript.

Funding: This research is part of the project “TED2021-130461B-I00” funded by the European Union “NextGenerationEU”/PRTR and the Spanish Ministerio de Ciencias, Innovación y Universidades (MICIU/AEI/10.13039/501100011033).

Data Availability Statement: The data supporting this paper are available upon request from the corresponding authors.

Acknowledgments: The authors would like to thank the Ministerio de Ciencias, Innovación y Universidades and the Next Generation EU for funding the project that permitted them to carry out this study. The authors also want to acknowledge the Centres Científics i Tecnològics de la Universitat de Barcelona (CCiTUB) for sharing its facilities and its help in the surface and structural characterization of the materials.

Conflicts of Interest: The authors declare no conflicts of interest.

References

1. Bareiß, K.; De La Rúa, C.; Möckl, M.; Hamacher, T. Life Cycle Assessment of Hydrogen from Proton Exchange Membrane Water Electrolysis in Future Energy Systems. *Appl. Energy* **2019**, *237*, 862–872. [CrossRef]
2. Zohuri, B. *Hydrogen Energy: Challenges and Solutions for a Cleaner Future*; Springer International Publishing: Cham, Switzerland, 2019; ISBN 978-3-319-93460-0.
3. Nikolaidis, P.; Poullikkas, A. A Comparative Overview of Hydrogen Production Processes. *Renew. Sustain. Energy Rev.* **2017**, *67*, 597–611. [CrossRef]
4. Awad, M.; Said, A.; Saad, M.H.; Farouk, A.; Mahmoud, M.M.; Alshammari, M.S.; Alghaythi, M.L.; Abdel Aleem, S.H.E.; Abdelaziz, A.Y.; Omar, A.I. A Review of Water Electrolysis for Green Hydrogen Generation Considering PV/Wind/Hybrid/Hydropower/Geothermal/Tidal and Wave/Biogas Energy Systems, Economic Analysis, and Its Application. *Alex. Eng. J.* **2024**, *87*, 213–239. [CrossRef]
5. Hou, J.; Yang, M. *Green Hydrogen Production by Water Electrolysis*, 1st ed.; CRC Press: Boca Raton, FL, USA, 2024; ISBN 978-1-003-36893-9.
6. El-Shafie, M. Hydrogen Production by Water Electrolysis Technologies: A Review. *Results Eng.* **2023**, *20*, 101426. [CrossRef]
7. Molera, M.; Sarret, M.; Fàbrega, C.; Andreu, T. Effect of Light and Electrode Polarization on BiVO₄ and TiO₂ Photoanodes for Glycerol Oxidation. *J. Electrochem. Soc.* **2024**, *171*, 086503. [CrossRef]
8. Rakousky, C.; Shviro, M.; Carmo, M.; Stolten, D. Iridium Nanoparticles for the Oxygen Evolution Reaction: Correlation of Structure and Activity of Benchmark Catalyst Systems. *Electrochim. Acta* **2019**, *302*, 472–477. [CrossRef]
9. Dawood, F.; Anda, M.; Shafiullah, G.M. Hydrogen Production for Energy: An Overview. *Int. J. Hydrogen Energy* **2020**, *45*, 3847–3869. [CrossRef]
10. Wang, S.; Lu, A.; Zhong, C.-J. Hydrogen Production from Water Electrolysis: Role of Catalysts. *Nano Converg.* **2021**, *8*, 4. [CrossRef]
11. Cabot, P.L.; Martínez-Huerta, M.V.; Alcaide, F. Advanced Supports for Noble Metal Catalysts in Proton Exchange Membrane Water Electrolysers: A Review: Improving the Performance, Stability, Durability and Cost of Iridium- and Platinum-Based Catalytic Materials. *Johns. Matthey Technol. Rev.* **2023**, *67*, 249–265. [CrossRef]
12. Mirshekari, G.; Ouimet, R.; Zeng, Z.; Yu, H.; Bliznakov, S.; Bonville, L.; Niedzwiecki, A.; Capuano, C.; Ayers, K.; Maric, R. High-Performance and Cost-Effective Membrane Electrode Assemblies for Advanced Proton Exchange Membrane Water Electrolyzers: Long-Term Durability Assessment. *Int. J. Hydrogen Energy* **2021**, *46*, 1526–1539. [CrossRef]

13. Chen, Z.; Guo, L.; Pan, L.; Yan, T.; He, Z.; Li, Y.; Shi, C.; Huang, Z.; Zhang, X.; Zou, J. Advances in Oxygen Evolution Electrocatalysts for Proton Exchange Membrane Water Electrolyzers. *Adv. Energy Mater.* **2022**, *12*, 2103670. [CrossRef]
14. Stähler, M.; Stähler, A.; Scheepers, F.; Carmo, M.; Stolten, D. A Completely Slot Die Coated Membrane Electrode Assembly. *Int. J. Hydrogen Energy* **2019**, *44*, 7053–7058. [CrossRef]
15. Jiang, G.; Yu, H.; Li, Y.; Yao, D.; Chi, J.; Sun, S.; Shao, Z. Low-Loading and Highly Stable Membrane Electrode Based on an Ir@WO_x NR Ordered Array for PEM Water Electrolysis. *ACS Appl. Mater. Interfaces* **2021**, *13*, 15073–15082. [CrossRef]
16. Holzapfel, P.; Bühler, M.; Van Pham, C.; Hegge, F.; Böhm, T.; McLaughlin, D.; Breitwieser, M.; Thiele, S. Directly Coated Membrane Electrode Assemblies for Proton Exchange Membrane Water Electrolysis. *Electrochem. Commun.* **2020**, *110*, 106640. [CrossRef]
17. Stähler, M.; Stähler, A.; Scheepers, F.; Carmo, M.; Lehnert, W.; Stolten, D. Impact of Porous Transport Layer Compression on Hydrogen Permeation in PEM Water Electrolysis. *Int. J. Hydrogen Energy* **2020**, *45*, 4008–4014. [CrossRef]
18. Bühler, M.; Hegge, F.; Holzapfel, P.; Bierling, M.; Suermann, M.; Vierrath, S.; Thiele, S. Optimization of Anodic Porous Transport Electrodes for Proton Exchange Membrane Water Electrolyzers. *J. Mater. Chem. A* **2019**, *7*, 26984–26995. [CrossRef]
19. Klose, C.; Trinke, P.; Böhm, T.; Bensmann, B.; Vierrath, S.; Hanke-Rauschenbach, R.; Thiele, S. Membrane Interlayer with Pt Recombination Particles for Reduction of the Anodic Hydrogen Content in PEM Water Electrolysis. *J. Electrochem. Soc.* **2018**, *165*, F1271–F1277. [CrossRef]
20. Millet, P.; Mbemba, N.; Grigoriev, S.A.; Fateev, V.N.; Aukauloo, A.; Etiévant, C. Electrochemical Performances of PEM Water Electrolysis Cells and Perspectives. *Int. J. Hydrogen Energy* **2011**, *36*, 4134–4142. [CrossRef]
21. Ren, W.; Wang, K.; Lu, D.; Xu, C. High-Stability RuO₂/MoO₃ Electrocatalyst for the Oxygen Evolution Reaction in Proton-Exchange-Membrane Water Electrolysis. *ACS Appl. Energy Mater.* **2023**, *6*, 12573–12578. [CrossRef]
22. Man, I.C.; Su, H.; Calle-Vallejo, F.; Hansen, H.A.; Martínez, J.I.; Inoglu, N.G.; Kitchin, J.; Jaramillo, T.F.; Nørskov, J.K.; Rossmeisl, J. Universality in Oxygen Evolution Electrocatalysis on Oxide Surfaces. *ChemCatChem* **2011**, *3*, 1159–1165. [CrossRef]
23. Reier, T.; Nong, H.N.; Teschner, D.; Schlögl, R.; Strasser, P. Electrocatalytic Oxygen Evolution Reaction in Acidic Environments—Reaction Mechanisms and Catalysts. *Adv. Energy Mater.* **2017**, *7*, 1601275. [CrossRef]
24. Daily Metal Price: Iridium Price (USD/Kilogram) for the Last Month. Available online: <https://www.dailymetalprice.com/metalprices.php> (accessed on 20 August 2024).
25. Orth, C.J.; Attrep, M.; Quintana, L.R. Iridium Abundance Patterns across Bio-Event Horizons in the Fossil Record. In *Geological Society of America Special Papers*; Geological Society of America: Boulder, CO, USA, 1990; Volume 247, pp. 45–60, ISBN 978-0-8137-2247-4.
26. Rozain, C.; Mayousse, E.; Guillet, N.; Millet, P. Influence of Iridium Oxide Loadings on the Performance of PEM Water Electrolysis Cells: Part I—Pure IrO₂-Based Anodes. *Appl. Catal. B Environ.* **2016**, *182*, 153–160. [CrossRef]
27. Rozain, C.; Mayousse, E.; Guillet, N.; Millet, P. Influence of Iridium Oxide Loadings on the Performance of PEM Water Electrolysis Cells: Part II—Advanced Oxygen Electrodes. *Appl. Catal. B Environ.* **2016**, *182*, 123–131. [CrossRef]
28. Pham, C.V.; Bühler, M.; Knöppel, J.; Bierling, M.; Seeberger, D.; Escalera-López, D.; Mayrhofer, K.J.J.; Cherevko, S.; Thiele, S. IrO₂ Coated TiO₂ Core-Shell Microparticles Advance Performance of Low Loading Proton Exchange Membrane Water Electrolyzers. *Appl. Catal. B Environ.* **2020**, *269*, 118762. [CrossRef]
29. Bernt, M.; Siebel, A.; Gasteiger, H.A. Analysis of Voltage Losses in PEM Water Electrolyzers with Low Platinum Group Metal Loadings. *J. Electrochem. Soc.* **2018**, *165*, F305–F314. [CrossRef]
30. Li, G.; Xu, X.; Liu, H.; Yang, X.; Lin, M. Enhanced Electrocatalytic Performance of IrO_x by Employing F-Doped TiO₂ as Support towards Acidic Oxygen Evolution Reaction. *ChemCatChem* **2022**, *14*, e202201039. [CrossRef]
31. Oh, H.-S.; Nong, H.N.; Reier, T.; Bergmann, A.; Glied, M.; Ferreira De Araújo, J.; Willinger, E.; Schlögl, R.; Teschner, D.; Strasser, P. Electrochemical Catalyst–Support Effects and Their Stabilizing Role for IrO_x Nanoparticle Catalysts during the Oxygen Evolution Reaction. *J. Am. Chem. Soc.* **2016**, *138*, 12552–12563. [CrossRef]
32. Oakton, E.; Lebedev, D.; Povia, M.; Abbott, D.F.; Fabbri, E.; Fedorov, A.; Nachttegaal, M.; Copéret, C.; Schmidt, T.J. IrO₂-TiO₂: A High-Surface-Area, Active, and Stable Electrocatalyst for the Oxygen Evolution Reaction. *ACS Catal.* **2017**, *7*, 2346–2352. [CrossRef]
33. Fang, Z.; Tang, Z.; Lin, S.; Li, R.; Chen, X.; Tian, J.; Liu, L.; Peng, J.; Liu, S.; Fu, B.; et al. Doped TiO₂-Supported IrO₂ Electrocatalysts with High Activity and Durability toward the Acidic Oxygen Evolution Reaction. *CrystEngComm* **2024**, *26*, 475–483. [CrossRef]
34. Moriau, L.; Smiljanić, M.; Lončar, A.; Hodnik, N. Supported Iridium-based Oxygen Evolution Reaction Electrocatalysts—Recent Developments. *ChemCatChem* **2022**, *14*, e202200586. [CrossRef]
35. Lettieri, S.; Pavone, M.; Fioravanti, A.; Santamaria Amato, L.; Maddalena, P. Charge Carrier Processes and Optical Properties in TiO₂ and TiO₂-Based Heterojunction Photocatalysts: A Review. *Materials* **2021**, *14*, 1645. [CrossRef]
36. Genova-Koleva, R.V.; Alcaide, F.; Álvarez, G.; Cabot, P.L.; Grande, H.-J.; Martínez-Huerta, M.V.; Miguel, O. Supporting IrO₂ and IrRuO Nanoparticles on TiO₂ and Nb-Doped TiO₂ Nanotubes as Electrocatalysts for the Oxygen Evolution Reaction. *J. Energy Chem.* **2019**, *34*, 227–239. [CrossRef]
37. Nah, Y.; Paramasivam, I.; Schmuki, P. Doped TiO₂ and TiO₂ Nanotubes: Synthesis and Applications. *ChemPhysChem* **2010**, *11*, 2698–2713. [CrossRef] [PubMed]

38. You, H.; Wu, Q.; Li, J.; He, S.; Li, X.; Yang, X.; Yang, J.; Meng, Y.; Tong, S.; Wu, M. Hollow Nanocubes Constructed from Oriented Anatase TiO₂ Nanoarrays: Topotactic Conversion and Fast Lithium-Ion Storage. *CrystEngComm* **2017**, *19*, 2456–2463. [[CrossRef](#)]
39. Roy, P.; Berger, S.; Schmuki, P. TiO₂ Nanotubes: Synthesis and Applications. *Angew. Chem. Int. Ed.* **2011**, *50*, 2904–2939. [[CrossRef](#)] [[PubMed](#)]
40. Reghunath, S.; Pinheiro, D.; Kr, S.D. A Review of Hierarchical Nanostructures of TiO₂: Advances and Applications. *Appl. Surf. Sci. Adv.* **2021**, *3*, 100063. [[CrossRef](#)]
41. Hu, J.Z.; Deng, P.C.; Wang, X.W.; Xu, H.B. Stable Ti/IrO₂ Anode with Iridium-Titanium Oxide Interlayers for O₂ Evolution. *Mater. Sci. Forum* **2011**, *694*, 662–666. [[CrossRef](#)]
42. Massué, C.; Pfeifer, V.; Huang, X.; Noack, J.; Tarasov, A.; Cap, S.; Schlögl, R. High-Performance Supported Iridium Oxohydroxide Water Oxidation Electrocatalysts. *ChemSusChem* **2017**, *10*, 1943–1957. [[CrossRef](#)] [[PubMed](#)]
43. Karade, S.S.; Sharma, R.; Gyergyek, S.; Morgen, P.; Andersen, S.M. IrO₂/Ir Composite Nanoparticles (IrO₂@Ir) Supported on TiN_xO_y Coated TiN: Efficient and Robust Oxygen Evolution Reaction Catalyst for Water Electrolysis. *ChemCatChem* **2023**, *15*, e202201470. [[CrossRef](#)]
44. Tian, F.; Zhang, Y.; Zhang, J.; Pan, C. Raman Spectroscopy: A New Approach to Measure the Percentage of Anatase TiO₂ Exposed (001) Facets. *J. Phys. Chem. C* **2012**, *116*, 7515–7519. [[CrossRef](#)]
45. Ohsaka, T.; Izumi, F.; Fujiki, Y. Raman Spectrum of Anatase, TiO₂. *J. Raman Spectrosc.* **1978**, *7*, 321–324. [[CrossRef](#)]
46. Li, G.; Li, K.; Yang, L.; Chang, J.; Ma, R.; Wu, Z.; Ge, J.; Liu, C.; Xing, W. Boosted Performance of Ir Species by Employing TiN as the Support toward Oxygen Evolution Reaction. *ACS Appl. Mater. Interfaces* **2018**, *10*, 38117–38124. [[CrossRef](#)]
47. Guo, H.; Fang, Z.; Li, H.; Fernandez, D.; Henkelman, G.; Humphrey, S.M.; Yu, G. Rational Design of Rhodium–Iridium Alloy Nanoparticles as Highly Active Catalysts for Acidic Oxygen Evolution. *ACS Nano* **2019**, *13*, 13225–13234. [[CrossRef](#)] [[PubMed](#)]
48. Jang, H.; Lee, J.-H.; Lee, J.R.; Kim, T.-W. Metal–Support Interaction Can Deactivate IrO_x/Sb:SnO₂ OER Catalysts in Polyol Process. *ACS Appl. Energy Mater.* **2022**, *5*, 9297–9302. [[CrossRef](#)]
49. Hao, C.; Lv, H.; Mi, C.; Song, Y.; Ma, J. Investigation of Mesoporous Niobium-Doped TiO₂ as an Oxygen Evolution Catalyst Support in an SPE Water Electrolyzer. *ACS Sustain. Chem. Eng.* **2016**, *4*, 746–756. [[CrossRef](#)]
50. Hu, W.; Chen, S.; Xia, Q. IrO₂/Nb–TiO₂ Electrocatalyst for Oxygen Evolution Reaction in Acidic Medium. *Int. J. Hydrogen Energy* **2014**, *39*, 6967–6976. [[CrossRef](#)]
51. Burke, L.D.; Whelan, D.P. A Voltammetric Investigation of the Charge Storage Reactions of Hydrated Iridium Oxide Layers. *J. Electroanal. Chem. Interfacial Electrochem.* **1984**, *1–2*, 121–141. [[CrossRef](#)]
52. Siracusano, S.; Di Blasi, A.; Baglio, V.; Brunaccini, G.; Briguglio, N.; Stassi, A.; Ornelas, R.; Trifoni, E.; Antonucci, V.; Aricò, A.S. Optimization of Components and Assembling in a PEM Electrolyzer Stack. *Int. J. Hydrogen Energy* **2011**, *36*, 3333–3339. [[CrossRef](#)]
53. Jia, A.; Zhang, Y.; Song, T.; Hu, Y.; Zheng, W.; Luo, M.; Lu, J.; Huang, W. The Effects of TiO₂ Crystal-Plane-Dependent Ir–TiO Interactions on the Selective Hydrogenation of Crotonaldehyde over Ir/TiO₂ Catalysts. *Chin. J. Catal.* **2021**, *42*, 1742–1754. [[CrossRef](#)]
54. Noel, M.; Vasu, K.I. *Cyclic Voltammetry and the Frontiers of Electrochemistry*; Aspect Publications: London, UK, 1990; pp. 431–467, ISBN 978-1-85529-025-9.
55. Liu, J.; Wang, J.; Xu, C.; Jiang, H.; Li, C.; Zhang, L.; Lin, J.; Shen, Z.X. Advanced Energy Storage Devices: Basic Principles, Analytical Methods, and Rational Materials Design. *Adv. Sci.* **2018**, *5*, 1700322. [[CrossRef](#)]
56. Audichon, T.; Mayousse, E.; Morisset, S.; Morais, C.; Comminges, C.; Napporn, T.W.; Kokoh, K.B. Electroactivity of RuO₂–IrO₂ Mixed Nanocatalysts toward the Oxygen Evolution Reaction in a Water Electrolyzer Supplied by a Solar Profile. *Int. J. Hydrogen Energy* **2014**, *39*, 16785–16796. [[CrossRef](#)]
57. Ardizzone, S.; Fregonara, G.; Trasatti, S. “Inner” and “Outer” Active Surface of RuO₂ Electrodes. *Electrochim. Acta* **1990**, *35*, 263–267. [[CrossRef](#)]
58. McCrory, C.C.L.; Jung, S.; Peters, J.C.; Jaramillo, T.F. Benchmarking Heterogeneous Electrocatalysts for the Oxygen Evolution Reaction. *J. Am. Chem. Soc.* **2013**, *135*, 16977–16987. [[CrossRef](#)]
59. Lim, S.; Cho, J.; Park, S. Elevating IrO_x Acidic Oxygen Evolution Activity Using SnO₂-rGO Hybrid Support. *J. Electroanal. Chem.* **2023**, *928*, 116992. [[CrossRef](#)]
60. Siracusano, S.; Baglio, V.; D’Urso, C.; Antonucci, V.; Aricò, A.S. Preparation and Characterization of Titanium Suboxides as Conductive Supports of IrO₂ Electrocatalysts for Application in SPE Electrolysers. *Electrochim. Acta* **2009**, *54*, 6292–6299. [[CrossRef](#)]
61. Faria, L.A.D.; Boodts, J.F.C.; Trasatti, S. Electrocatalytic Properties of Ternary Oxide Mixtures of Composition Ru_{0.3}Ti_(0.7-x)Ce_xO₂: Oxygen Evolution from Acidic Solution. *J. Appl. Electrochem.* **1996**, *26*, 1195–1199. [[CrossRef](#)]
62. Corona-Guinto, J.L.; Cardeño-García, L.; Martínez-Casillas, D.C.; Sandoval-Pineda, J.M.; Tamayo-Meza, P.; Silva-Casarin, R.; González-Huerta, R.G. Performance of a PEM Electrolyzer Using RuIrCoO_x Electrocatalysts for the Oxygen Evolution Electrode. *Int. J. Hydrogen Energy* **2013**, *38*, 12667–12673. [[CrossRef](#)]
63. Tsuji, E.; Imanishi, A.; Fukui, K.; Nakato, Y. Electrocatalytic Activity of Amorphous RuO₂ Electrode for Oxygen Evolution in an Aqueous Solution. *Electrochim. Acta* **2011**, *56*, 2009–2016. [[CrossRef](#)]

64. Reier, T.; Teschner, D.; Lunkenbein, T.; Bergmann, A.; Selve, S.; Kraehnert, R.; Schlögl, R.; Strasser, P. Electrocatalytic Oxygen Evolution on Iridium Oxide: Uncovering Catalyst-Substrate Interactions and Active Iridium Oxide Species. *J. Electrochem. Soc.* **2014**, *161*, F876–F882. [[CrossRef](#)]
65. Hu, J.-M.; Zhang, J.-Q.; Cao, C.-N. Oxygen Evolution Reaction on IrO₂-Based DSA[®] Type Electrodes: Kinetics Analysis of Tafel Lines and EIS. *Int. J. Hydrogen Energy* **2004**, *29*, 791–797. [[CrossRef](#)]
66. Anantharaj, S.; Karthik, P.E.; Noda, S. The Significance of Properly Reporting Turnover Frequency in Electrocatalysis Research. *Angew. Chem. Int. Ed.* **2021**, *60*, 23051–23067. [[CrossRef](#)]
67. Shi, X.; Peng, H.-J.; Hersbach, T.J.P.; Jiang, Y.; Zeng, Y.; Baek, J.; Winther, K.T.; Sokaras, D.; Zheng, X.; Bajdich, M. Efficient and Stable Acidic Water Oxidation Enabled by Low-Concentration, High-Valence Iridium Sites. *ACS Energy Lett.* **2022**, *7*, 2228–2235. [[CrossRef](#)]
68. Abbott, D.F.; Lebedev, D.; Waltar, K.; Povia, M.; Nachttegaal, M.; Fabbri, E.; Copéret, C.; Schmidt, T.J. Iridium Oxide for the Oxygen Evolution Reaction: Correlation between Particle Size, Morphology, and the Surface Hydroxo Layer from Operando XAS. *Chem. Mater.* **2016**, *28*, 6591–6604. [[CrossRef](#)]
69. Islam, N.; Moushumi, Z.M.; Islam, M.R.; Hossain, M.I.; Rahman, M.A.; Rahaman, M.; Aldalbahi, A.; Uddin, T.; Singha, N.R.; Hasnat, M.A. Activation of Stannic Oxide by the Incorporation of Ruthenium Oxide Nanoparticles for Efficient Hydrogen Evolution Reaction. *Electrochim. Acta* **2024**, *507*, 145114. [[CrossRef](#)]
70. Miranda, M.A.R.; Sasaki, J.M. The Limit of Application of the Scherrer Equation. *Acta Crystallogr. Sect. Found. Adv.* **2018**, *74*, 54–65. [[CrossRef](#)]
71. Monshi, A.; Foroughi, M.R.; Monshi, M.R. Modified Scherrer Equation to Estimate More Accurately Nano-Crystallite Size Using XRD. *World J. Nano Sci. Eng.* **2012**, *2*, 154–160. [[CrossRef](#)]

Disclaimer/Publisher's Note: The statements, opinions and data contained in all publications are solely those of the individual author(s) and contributor(s) and not of MDPI and/or the editor(s). MDPI and/or the editor(s) disclaim responsibility for any injury to people or property resulting from any ideas, methods, instructions or products referred to in the content.